Article

Synergy of dual-atom catalysts deviated from the scaling relationship for oxygen evolution reaction

Cong Fang[1,2], Jian Zhou[1,2,3], Lili Zhang[1,2,3], Wenchao Wan[4], Yuxiao Ding [3,5] & Xiaoyan Sun [1,2,3]

Dual-atom catalysts, particularly those with heteronuclear active sites, have the potential to outperform the well-established single-atom catalysts for oxygen evolution reaction, but the underlying mechanistic understanding is still lacking. Herein, a large-scale density functional theory is employed to explore the feasibility of *O-*O coupling mechanism, which can circumvent the scaling relationship with improving the catalytic performance of N-doped graphene supported Fe-, Co-, Ni-, and Cu-containing heteronuclear dual-atom catalysts, namely, M'M@NC. Based on the constructed activity maps, a rationally designed descriptor can be obtained to predict homonuclear catalysts. Seven heteronuclear and four homonuclear dual-atom catalysts possess high activities that outperform the minimum theoretical overpotential. The chemical and structural origin in favor of *O-*O coupling mechanism thus leading to enhanced reaction activity have been revealed. This work not only provides additional insights into the fundamental understanding of reaction mechanisms, but also offers a guideline for the accelerated discovery of efficient catalysts.

Oxygen evolution reaction (OER) is a vital process for water splitting, fuel cells, and metal-air batteries[1–3]. Essentially, the OER process is a thermodynamically uphill reaction with multi-step proton-coupled electron transfer, and the sluggish kinetics requires high-performance catalysts to reduce the reaction overpotential for practical applications[4–6]. IrO_2 and RuO_2, the present state-of-the-art OER catalysts[7–9], exhibit high OER activity but must be replaced due to high cost and lack of stability in order to facilitate wider practical applications[10]. A grant challenge for electrocatalysis is the design of OER electrocatalysts with high activity and durable stability.

Recently, an increasing amount of research has focused on single-atom catalysts (SACs) that inherit the advantages of both homogeneous and heterogeneous catalysts[11,12], particularly in N-doped graphene-supported single transition metal atoms (M–N–C)[13,14]. Extension has been made from single intermediate electrochemical reactions i.e. the hydrogen evolution reaction (HER)[15] to multi-intermediate electrochemical reactions, such as oxygen reduction reaction (ORR)[16–18], nitrate reduction reaction (NO_3RR)[19], oxygen evolution reaction (OER)[20], and CO_2 reduction reaction (CO_2RR)[21–26]. This can be attributed to the benefits of SACs, which include an unsaturated coordination configuration, maximal metal utilization, and relatively uniform active sites[27]. However, the individual active sites determine the fixed adsorption mode, which is tightly correlated with the adsorption energy of multi-step reaction intermediates bonding on a single center. Especially for specific multi-step reactions like the OER process, the presence of a linear scaling relationship makes it rather challenging to simultaneously optimize and tune the adsorption of each oxygenated intermediate

[1]Qingdao Institute of Bioenergy and Bioprocess Technology, Chinese Academy of Sciences, 266101 Qingdao, China. [2]Shandong Energy Institute, 266101 Qingdao, China. [3]University of Chinese Academy of Sciences, 100049 Beijing, China. [4]Max-Plank Institute for Chemical Energy Conversion, Mülheim an der Ruhr 45470, Germany. [5]Lanzhou Institute of Chemical Physics, Chinese Academy of Sciences, 730000 Lanzhou, China. ✉e-mail: yuxiaoding@licp.cas.cn; sunxy@qibebt.ac.cn

species at the single active site[28], which seriously limits the design flexibility and catalytic activity[29].

Dual-atom catalysts (DACs), not only possess the advantages of SACs but also allow the tuning and optimization of multi-intermediate reactions owing to their synergistic effect, that is, more flexible dual-metal active sites can modulate the adsorption energy of specific intermediate species[30], which is well suited for complex catalytic processes with multiple reaction steps and intermediates. Experimental investigations have revealed that DACs could provide higher activity performance compared to SACs. For instance, atomically dispersed Ni–Zn pairs obtained >90% CO Faraday efficiency across the broad potential window from −0.5 to −1.0 V (vs. RHE), and the synergistic effect enabled a CO_2 electron reduction performance superior to Ni/Zn single-metal sites[31]. Theoretically, graphene-based DACs (denoted as M′M@NC) were predicted to promote different reactions such as ORR[32–34], NRR[35–37], HER[38,39], and CO_2RR[40–42]. Regarding the OER process, several M′M@NCs with successful synthesis and application have been reported[43–45], for example, the Co–Ni pair exhibited high OER electrocatalytic activity and kinetics in alkaline conditions[46]. Moreover, P-doped FeNi@NC showed a low overpotential of 250 mV at a current density of 10 mA cm^{-2}[47]. Additionally, both DFT calculations[48,49] and machine learning[50–52] have made progress to explore and predict the superior performance of DACs in OER. Nevertheless, the combination of M_2 dimers experimentally applied to OER as well as the comprehensive and in-depth investigation of synergistic effects between metal–metal is still limited. In particular, the underlying reaction mechanism at the dual-metal active sites towards the enhanced OER activity remains to be further explored.

Recent studies have conclusively demonstrated that the contribution of unconventional mechanisms for electrocatalysis on the SACs cannot be overlooked and that deviations in scaling relationships significantly affect electrochemical activity, for instance, the formation of dihydride in HER[53], two *OH species in ORR and OER[54,55], as well as superoxo and peroxo complexes in OER[56]. Furthermore, the *O–*O coupling mechanism (OCM), as one of the unconventional mechanisms which were proposed on SACs[55], has also been shown with a remarkably different activity at the dual-metal active site from that of the conventional adsorption evolution mechanism (AEM)[48,57]. This is analogous to the direct coupling of adjacent oxygenated intermediates in the lattice oxygen mechanism (LOM), bypassing the generation of *OOH[58,59]. Moreover, unlike three-dimensional structured oxides that only allow the formation of *O–*O bonds on the surface due to the low bulk flexibility, the two-dimensional structure of graphene support can provide sufficient structural flexibility for the *O–*O coupling. Thus, one can reasonably assume that OER catalysis via OCM could potentially bypass the universal scaling relationship, leading to a lower reaction barrier and accelerated reaction kinetics[57,60]. From another point of view, DACs with two adjacent atomic metal species could act as one of the most representative platforms for directly investigating the chemical and structural origin of OCM.

However, to the best of our knowledge, there is still a lack of systematic study on screening and designing DACs following the OCM mechanism. In view of the myriad possible combinations of heteronuclear dimers, as well as the currently many unexplored DACs in the experiment, it is imperative to establish a feasible strategy, by which we could elucidate the fundamental factors in favor of OCM, popularize the advantages of OCM developed from valuable previous studies[54,55], and further predict the promising candidates with much improved OER activity. To this end, by means of large-scale density functional theory (DFT) calculations with a computational hydrogen electrode model, we herein established a series of heteronuclear diatomic catalysts (M′M@NC, M′ = Fe, Co, Ni, Cu, and M is ranging from Ti to Au) as well as homonuclear transition metal diatomic catalysts M_2@NC embedded on a two-dimensional N-doped graphene surface. We successfully screened out four homonuclear and seven

heteronuclear DACs exhibiting superior OER activity via OCM than the corresponding SACs and the benchmark of minimum theoretical overpotential. Particularly, the detailed analyses of the reaction paths and electronic features of those promising DACs enable us to propose a general strategy in favor of the *O–*O coupling mechanism for designing high-performance OER catalysts, which could guide further exploration of an even broader composition space of DACs for other related electrocatalytic reactions.

Results

Geometric structure and stability of heteronuclear DACs

Considering the synthesis strategies of FeM, CoM, NiM, and CuM have been well-established and extensively reported in recent experimental studies[61,62], here, we choose Fe, Co, Ni, and Cu as the candidates for M′. Meanwhile, the metal dopants of M range from 3d, 4d, and 5d transition metals from IVB to IB (except Tc) with a total of 82 heteronuclear DACs. As displayed in Fig. 1a, the two transition-metal atoms (M_2) in DACs joined and were both surrounded by three pyridine sp^2-N atoms. Previous theoretical investigations demonstrated that this is the most energetically favorable configuration for embedding M_2 dimers in N-doped graphene, and various advanced characterization techniques comprehensively confirmed the atomically dispersed M_2 on the N-doped graphene as well as the presence of atomic pairs[31]. Accordingly, reasonably constructed M′M@NC catalyst models with metal–metal bond lengths in the range of 2.09 Å (CoV) to 2.75 Å (CuZr) were calculated (Fig. 1b and Supplementary Table 2). The bond lengths ranking of partial M_2 dimers is CuM > NiM > CoM > FeM, which is associated with the atomic radii of Fe, Co, Ni, and Cu, while the remaining bond lengths of M_2 dimers are independent of the atomic radii. Moreover, the computed bond lengths between M_2 dimers are corroborated with recent experimental measurements, e.g., the bond lengths obtained from both experimental and DFT calculations for the Ni–Zn pair in NiZn@NC is 2.5 Å[31], and the experimentally observed value of Ni–Cu bond length is 2.40 Å, which is also in agreement with our calculated value of 2.409 Å[63]. Thus, the rationality of our theoretical approach and the reliability of the present DFT method can be validated. Evidently, the dual-metal active sites with appropriate bond lengths can be expected to be advantageous in promoting O–O coupling with a low energy barrier.

The Bader charge analyses were also used to verify the electronic structural features of M′M@NC. The results show (Fig. 1c and Supplementary Table 3) that a substantial amount of charge is transferred from the M_2 dimers to the N-doped graphene, and the charge density difference of the models represented by FeZr@NC and FePd@NC exhibit a redistribution of charge (Supplementary Fig. 1), which results in the formation of strong-polarized and hybridized metal-N bonds. In addition, the DACs of FeM, CoM, NiM, and CuM all show a significant decreasing trend of charge transfer from left to right in the same period, which is consistent with the tendency of electronegativity (Supplementary Table 4)[64], indicating that the increased number of unpaired electrons in metal atoms favors the charge transfer to the surrounding atoms. Moreover, the charges transferred to the coordinated N atoms from all 86 M_2 dimers are 1.02–2.21|e|, considerably larger than 0.80|e| reported in the literature[65], which enables the M_2 dimers to exhibit high oxidation states.

Then, we evaluated the thermodynamic and electrochemical stability of the M_2 dimers. The possibility of the uniform distribution was determined by calculating the binding energy (BE $= E_{M′M@NC} - E_{M′M} - E_{NC}$) and aggregation energy ($E_{agg} = BE - E_{coh}$, where E_{coh} is the cohesion energy of the metal atom in their crystal) of the heteronuclear M_2 dimers with N-doped graphene, as displayed in Fig. 1d and Supplementary Tables 5–9[37,41]. The results show that the majority of M_2 dimers possessed sufficiently negative BE, indicating strong M–N bonds formation between the dispersed M_2 dimers and the surrounding ligand environment, which consistent with Fig. 1c.
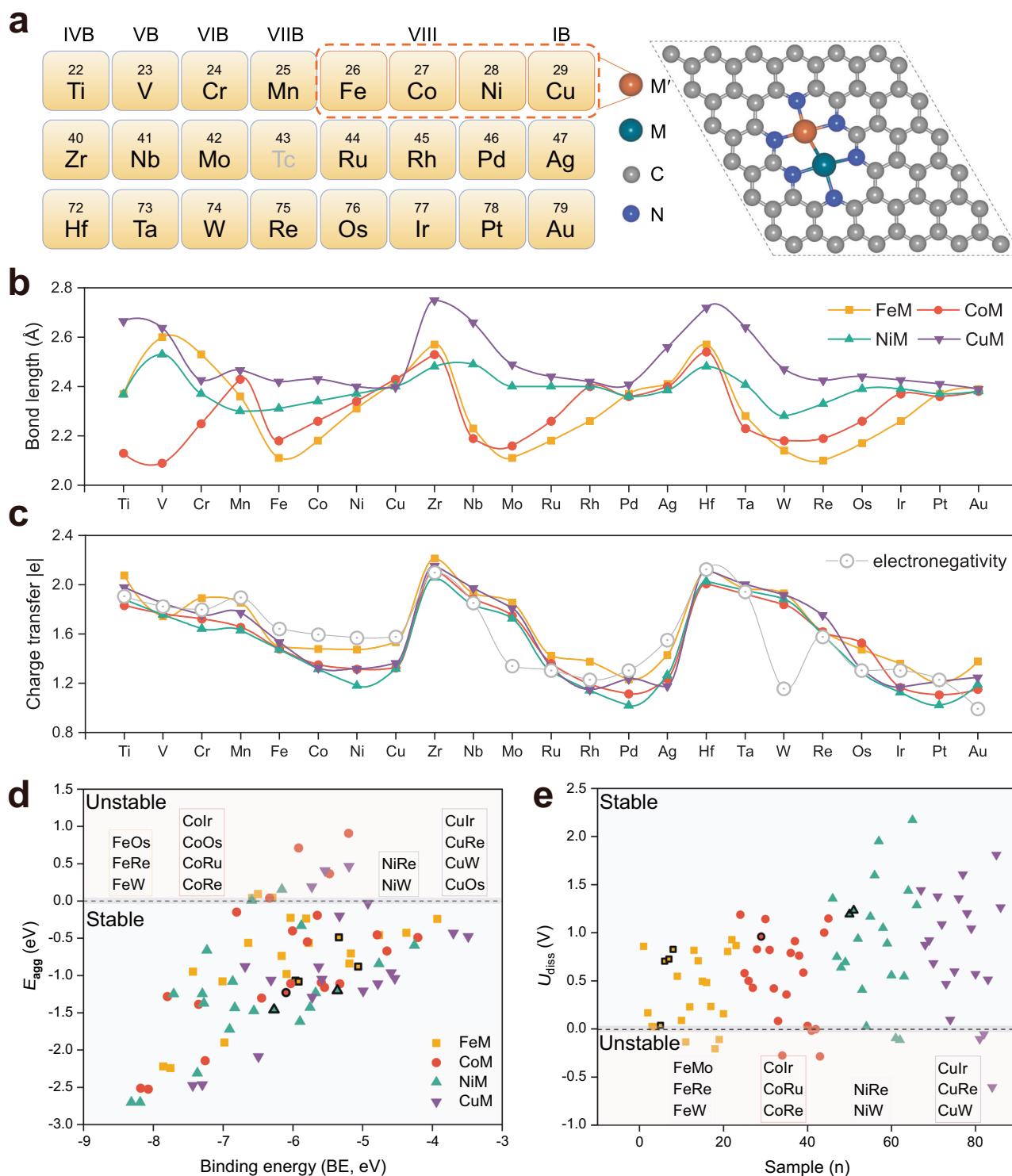
Fig. 1 | Structural prototype, bond length, charge transfer, and stability of M′M@NC. a Structural prototype of M′M@NC nanosheet. **b**, **c** Comparison of bond lengths and charge transfer of FeM, CoM, NiM, and CuM dimers on M′M@NC. **d** Computed binding energy (BE) and aggregation energy (E_{agg}) of metal dimers on N-doped graphene. **e** Calculated dissolution potential (U_{diss}) of M′M@NC at pH = 0, where the DACs systems highlighted in the black frame are the previously reported experimental ones (see discussion in the main text).

Furthermore, the calculated dissolution potential (U_{diss}) that applied to acidic solution show that most of the 86 M_2 dimers exhibited positive values in the range of 0–2.17 V (Fig. 1e and Supplementary Tables 10–13)[66], suggesting the stability of M_2 dimers in the acidic electrolyte and applied working potential environment under OER conditions. Overall, the M_2 dimers composed of FeM (Mo, W, Re and Os), CoM (Ru, Re, Os and Ir), NiM (Re and W), and CuM (W, Re, Os, and

Ir) need to be precautionarily averted in the experimental synthesis. Note that the DACs systems highlighted in black frame (Fig. 1d, e) are the reported experimentally synthesized metal dimers embedded in N-doped graphene, i.e., FeCo[67–69], FeNi[70–72], FeCu[73,74], CoNi[43,46], NiCu[63], Fe_2[75], and Ni_2[76,77], where BE, E_{agg}, and U_{diss} fulfill our evaluation criteria as mentioned above, further demonstrating the reliability and feasibility of our approach.
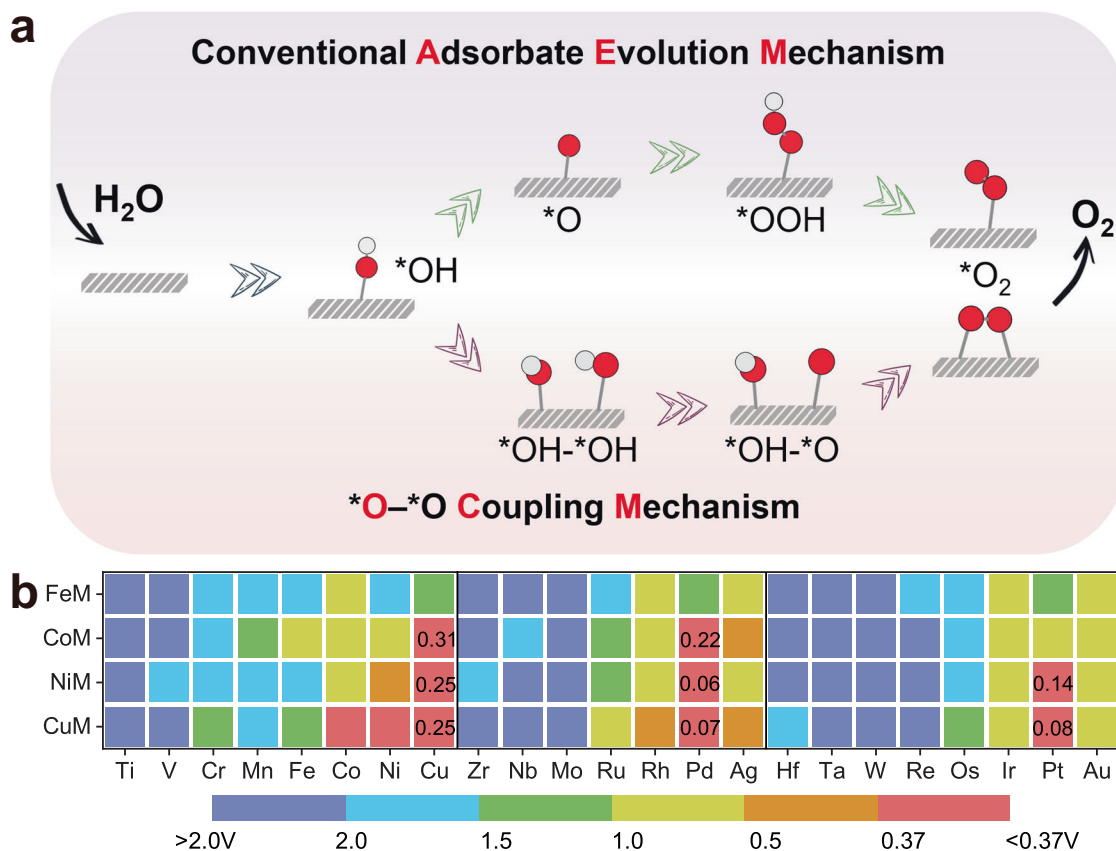
Fig. 2 | Reaction mechanisms and activity map. a Schematic illustration of the possible conventional adsorbate evolution mechanism (AEM) and O–O coupling mechanism (OCM). **b** The computed overpotential (η) of the FeM, CoM, NiM, and CuM dimers on M′M@NC.

OER pathways and activities of DACs

In the conventional AEM that proceeds at a single active center, the OER involves multiple oxygen reaction intermediates, including *OH, *O, and *OOH, as displayed in Fig. 2a. The binding energies of these intermediates are highly correlated, leading to a minimum theoretical overpotential of about 0.37 V[60]. In contrast, OCM with the introduction of a second active center can break the structural constraint on the crucial oxygenated intermediate. In this case, the most significant difference (Fig. 2a) is that two adjacent adsorbed oxygen atoms have the possibility to generate one oxygen molecule by direct *O–*O coupling through the steps Eqs. (11)–(20). The sequence of two *OH adsorption, as well as deprotonation on the M2 dimer, followed the energetically favorable configuration and the eventual release of the coupled oxygen molecule into the next reaction cycle (Supplementary Tables 14–29). In principle, without the involvement of *OOH intermediate, OCM could circumvent the scaling relationship, and become the remarkably favorable reaction pathways with the advantages of dual metal active sites.

To establish a database of a series of crucial factors such as OER activity and adsorption of key intermediates, the potential energy surfaces of 86 DACs systems (FeM, CoM, NiM, and CuM) based on pre-selected OCM pathways were systematically explored. The bottleneck of the AEM mechanism ($\eta = 0.37$ V) was used as a benchmark to manifest the high-performance OER catalysts and activity trends in the form of a heat map, as displayed in Fig. 2b and Supplementary Tables 30–60. Eight DACs meeting this benchmark were screened using $\eta < 0.37$ V, and they exhibited appreciable catalytic activities toward the OER as NiPd (0.06 V) < CuPd (0.07 V) < CuPt (0.08 V) < NiPt (0.14 V) < CoPd (0.22 V) < NiCu (0.25 V) = CuCu (0.25 V) < CoCu (0.31 V), the computed total energies of oxygenated intermediates,

zero-point energy correction, and entropy contribution energy are shown in Supplementary Tables S31–S38. Interestingly, it is also clear in the heat map from left to right, the area of the red/blue area gradually increases/decreases, whereas the red area represents a lower η. Accordingly, the M_2 dimers composed of early-transition metals will hinder the progress of OER, either FeM@NC, CoM@NC, NiM@NC, and CuM@NC are not conducive to the performance. In contrast, M_2 dimers with the late-transition metals, especially these noble metals Pd, Pt, and Au, exhibit excellent OER activity and are well below 0.37 V via OCM reported so far. Note that CoNi@NC was experimentally reported with a low overpotential of 252 mV at 10 mA cm^{-2}, and not included in our screened systems[46], which is probably related to the different reaction mechanisms actually followed.

The eight M_2 dimers combinations with $\eta < 0.37$ V were further compared to the corresponding M@NC (M = Co, Ni, Cu, Pd, and Pt) with similar N coordination environments to elucidate the activity differences between DACs and SACs, as well as the correlation between the synergistic effect of dual metal active site and structural engineering (Fig. 3 and Supplementary Figs. 2, 3). The computed total energy of oxygenated intermediates, zero-point energy correction, and entropy contribution energy of M@NC are given in Supplementary Tables 39–43. Based on the analysis of Gibbs free energy diagrams, potential determining steps (PDSs) of DACs following the OCM pathway can be found to primarily occur in the *O–*O coupling to generate *O$_2$ (Eqs. (14) or (19)), while the PDS of the six M@NC happens in the deprotonation of *OH to generate *O (Eqs. (2) or (7)) and the combination of *OH (Eqs. (1) or (6)). It is worth noting that the OER activities of all eight DACs are much higher than that of the corresponding SACs. Taking the best performing NiPd@NC as an example (Fig. 3d), the two *OH adsorbed on NiPd@NC with the most energetically favorable
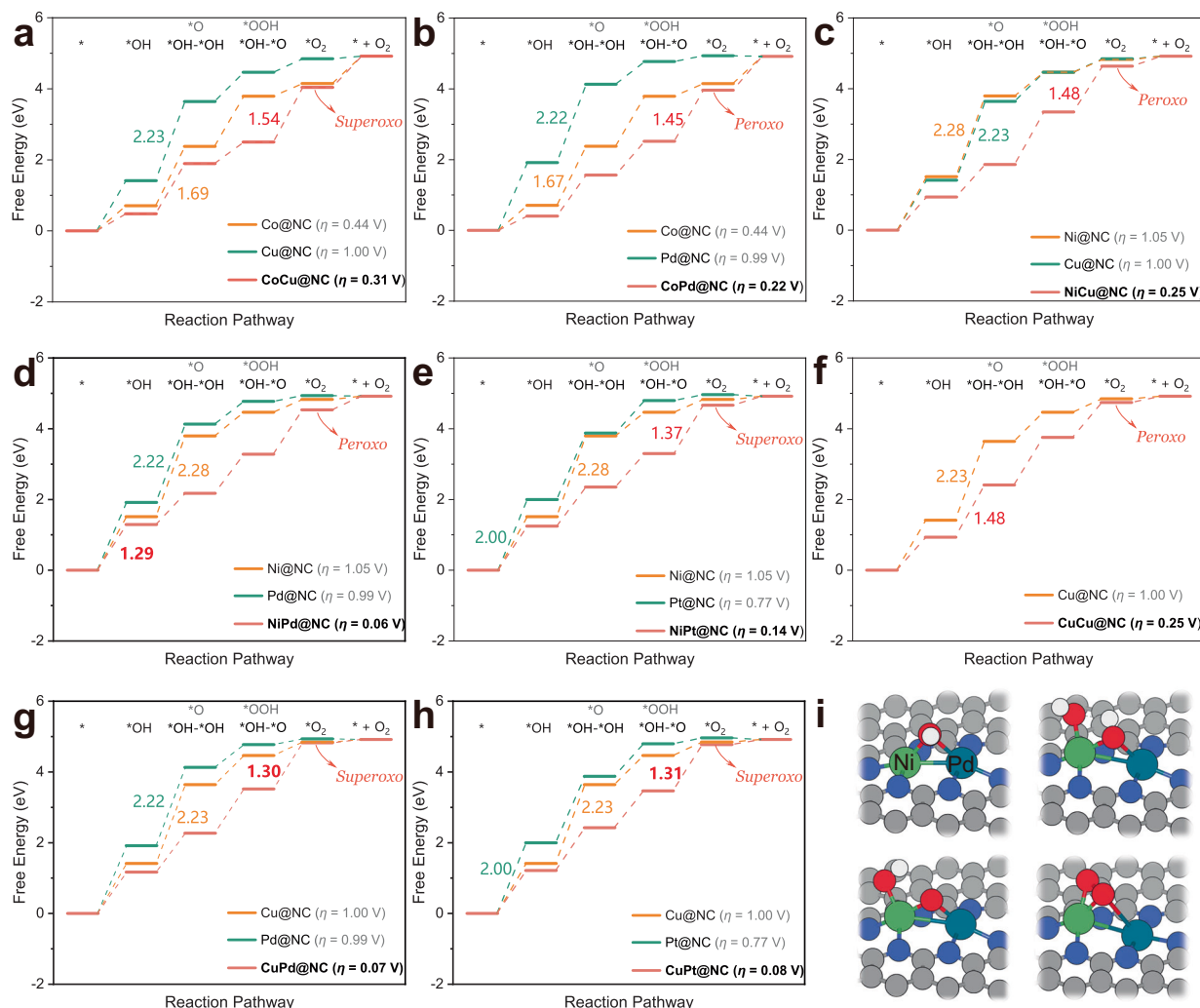
Fig. 3 | Gibbs free energy diagrams and optimized configurations. a–h Gibbs free energy diagrams of CoCu@NC, CoPd@NC, NiCu@NC, NiPd@NC, NiPt@NC, CuCu@NC, CuPd@NC, and CuPt@NC and the respective corresponding SACs for OER. **i** Optimized configurations of oxygenated intermediates represented as NiPd@NC. The white, red, gray, and blue spheres in the atomic models represent H, O, C, and N atoms, respectively.

conformation; then *OH on the bridge site firstly fulfills the deprotonation to form *OH–*O in the bridging-μ^2(M′, M) adsorption mode, which follows OCM with only slightly higher Gibbs free energy barrier than 1.23 eV to overcome the PDS (Eqs. (11) or (16)) and complete the reaction process. By contrast, Pd@NC and Ni@NC necessitate to overcome the Gibbs free energy barriers of 2.22 and 2.28 eV, respectively, to deprotonate *OH. To further verify the effectiveness of OCM, it is necessary to compare it with the conventional AEM for eight DACs (Supplementary Fig. 4 and Supplementary Tables 44–51). The PDS of NiPd@NC following AEM occurs at *OOH formation with a η of 1.06 V, which is significantly higher than that via OCM. The remaining seven DACs systems exhibit similar phenomena as NiPd@NC. As a result, not only the effective catalysis of OER by dual metal active sites along OCM is more beneficial, but also the synergistic effect between M_2 dimers significantly improves the reaction activity compared to SACs.

The above analysis of activity is based on the hypothesis that both *OH are adsorbed on the metal dimer, and whether alternative adsorption behavior is possible? For example, the second *OH adsorbs on the adjacent C site, or on the reverse side of the catalyst[48,55]. As shown in Supplementary Fig. 5a and Supplementary Tables 52–55, virtually the entire DACs, the second *OH prefers to adsorb at the M–M site compared to the M–C site, which circumvents the effect of the adjacent C site for *OH adsorption. Likewise, we also investigated the

possibility of the second *OH adsorption on the other side of the DACs, which can be achieved for nearly half of the 86 DACs (Supplementary Fig. 5b and Supplementary Tables 52–55). However, although the above calculations indicate the possibility of *OH adsorption on the reverse side, we used a monolayer model for DACs in this work, whereas experimentally synthesized graphene-based catalysts usually consist of multilayers[78], and not only intercalation effects need to be considered, such structures also prevent *O–*O coupling[55]. On the other hand, different combinations of metal dimers have various O affinities without assurance that the *OH on the other side will not undergo further evolution (e.g., *O and *OOH), which complicates the picture and is not considered in this work.

It is worth noting that *O2 → O2(g), as a non-electrochemical process[79], is not appropriate to be included in the elementary steps, which overestimates the overpotential and misjudges the PDS. Inspired by the literature[56], *O2 exhibits peroxide or superoxide characteristics in two different adsorption modes, end-on and side-on, respectively, due to the different combinations that induce variation in O-affinity. Supplementary Fig. 2 illustrates the specific adsorption configurations which are indicated in Fig. 3 as the peroxo- or superoxide nature of *O2. On the other hand, the desorption of *O2 was also evaluated for 86 DACs with a benchmark value of an experimentally reported DACs that follows OCM ($\Delta G_{*O2 \to O2(g)}$ = 1.17 eV)[57]. The
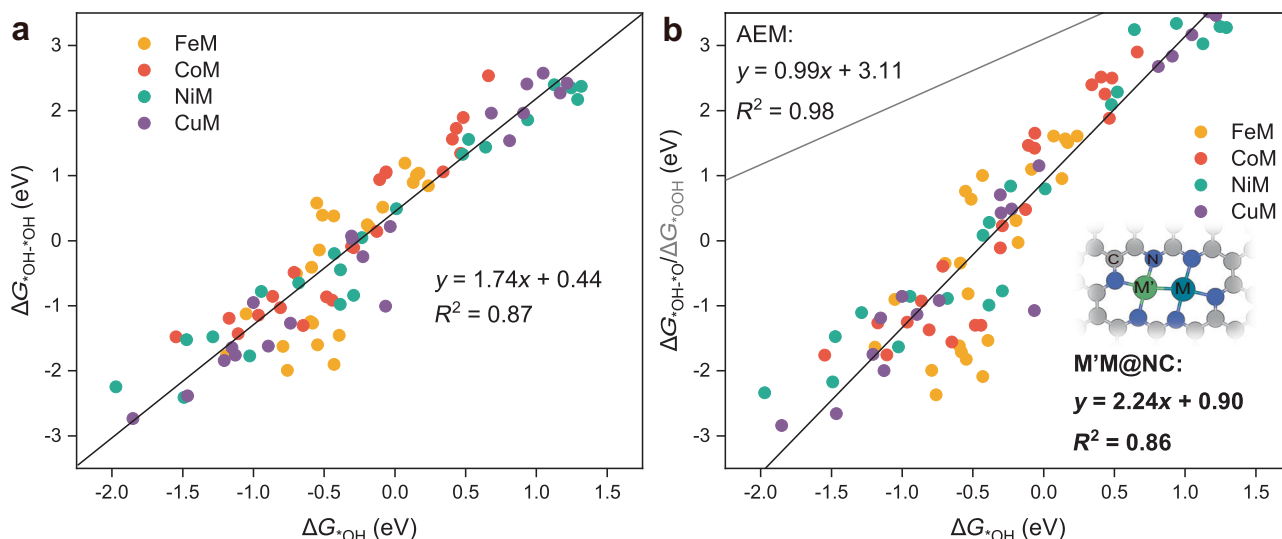
Fig. 4 | Scaling relationships following the OCM. a Relationship between ΔG_{*OH} and $\Delta G_{*OH-*OH}$ of M'M@NC. **b** Relationship between ΔG_{*OH} and ΔG_{*OH-*O} of M'M@NC. The gray line represents the scaling relationship following the AEM (containing SACs, DACs, and metal oxides, as shown in Supplementary Fig. 11). Inset shows the schematic configuration of M'M@NC.

excessive $\Delta G_{*O2\rightarrow O2(g)}$, i.e. higher than 1.17 eV, could be unfavorable for the reaction cycle, and it turns out that 8 high-performance DACs screened in the present study possess favorable desorption capacity with moderate O-affinity (Supplementary Table 56).

To better understand the significance of $*O_2$, a correlation between the charge amount of $*O_2$ received from the slab and the O–O bond length of $*O_2$ (Supplementary Fig. 6a) can be established, implying that the more charge $*O_2$ receives, the longer the bond length. Particularly, after excluding the disturbance data of DACs with $\Delta G_{*O2\rightarrow O2(g)} > 1.17$ eV, this linear correlation is more satisfactory (Supplementary Fig. 6b). Therefore, the O–O distance of $*O_2$ can be employed as a useful descriptor to describe the charge transfer. In addition, we also plotted the correlation with bond length and $\Delta G_{*O2\rightarrow O2(g)}$. Unfortunately, no strong correlation exists between the both, which is possibly caused by the wide energy range of the $\Delta G_{*O2\rightarrow O2(g)}$ (Supplementary Fig. 6c, d).

As the support also plays a vital role in electrochemical reactions[80], it is necessary to explore the activity of different support for the same metal dimers (FeM, CoM, NiM, and CuM). Two adjacent single vacancies on graphene accommodating metal dimers (M'M@Gr) were used as the prototype[81,82] (Supplementary Fig. 7) to further evaluate the support effect for the catalytic performance of DACs along the OCM. The activity trends of 86 M'M@Gr along the OCM for OER are shown as a heat map in Supplementary Fig. 8, with all oxygenated intermediates as the most stable configuration (Supplementary Tables 57–60). In analogy to Fig. 2b, the heat map also clearly shows a progressively improved activity from left to right, indicating that early-transition metal doping disadvantages the OER performance in either N-doped or defective graphene. In contrast to Fig. 2b, the quantities of DACs with high activity on defective graphene support are much less than that on N-doped graphene support, following the order FeFe(0.38 V) = CuPd(0.38 V) < CoAg(0.39 V) < NiCu(0.40 V) < CoPd(0.42 V) < CoCu(0.43 V) = CuCu(0.43 V) < NiAu(0.50 V). Based on the analysis of the free energy diagrams (Supplementary Fig. 9), the above 8 M'M@Gr exhibited strong adsorption of oxygenated intermediates, with consequently high overpotential and difficulty in O_2 desorption, thus unfavorable for the sustainability of reaction.

Exploration of homonuclear DACs for OER

It is well known that in the conventional AEM, the difference between the adsorption-free energy of $*OOH$ and $*OH$ ($\Delta G_{*OOH}-\Delta G_{*OH}$) for an ideal OER catalyst is 2.46 eV, enabling all four elementary steps in the same magnitude of reaction free energy. However, the virtually constant difference ($\Delta G_{*OOH} - \Delta G_{*OH}$) of 3.2 ± 0.2 eV on the single active site has determined the lowest theoretical overpotential of 0.37 V ([3.2−2.46 eV]/2)[60]. Based on the above large-scale screening along the OCM, eight highly active DACs have overcome the limitation of minimum theoretical overpotential of 0.37 V. Obviously, the scaling relationship of OCM should be distinguished from that of conventional AEM. Consequently, we plotted the correlation between the adsorption-free energies of $*OH$, $*OH-*OH$, $*OH-*O$, and $*O_2$. Interestingly, there is a significant linear correlation between the adsorption-free energy of $*OH$ (ΔG_{*OH}) and other oxygenated intermediates (Fig. 4 and Supplementary Fig. 10). Meanwhile, the dual metal active site followed the scaling relationship significantly deviated from that of the notably challenging AEM followed in Fig. 4b, without the constant difference of 3.2 ± 0.2 eV, which implicated that the minimum theoretical overpotential of 0.37 V was remarkably lowered by the dual metal active site, especially NiPd (0.06 V), CuPd (0.07 V) and CuPt (0.08 V). Notably, despite the fact that OER activity on M'M@Gr was inferior due to the excessively strong adsorption of oxygenated intermediates, the critical intermediates follow the same scaling relationship in Fig. 4b, albeit with different support (Supplementary Fig. 12), indicating a general rule of OCM on DACs.

The well-accepted Sabatier principle emphasizes that the binding of the adsorbed intermediates with the catalyst active site should be neither too strong nor too weak, both of which would impede the catalytic activity. $\Delta G_{*O} - \Delta G_{*OH}$ is generally employed as a descriptor for determining the OER activity in the volcano plot of AEM. Accordingly, we employed the similar descriptor $\Delta G_{*OH-*OH}$ for OCM to describe the catalytic behavior of OER on M_2@NC. Selection of descriptor is based on the fact that PDS occurs mainly in $*O-*O$ coupling that the adsorption of two $*OH$ determines the subsequent deprotonation as well as the $*O-*O$ coupling process. Interestingly, we found a volcano-shaped relationship between $\Delta G_{*OH-*OH}$ and η (Fig. 5a), in which the optimal overpotential occurs as 1.56 eV $< \Delta G_{*OH-*OH} <$ 2.46 eV, derived from eight DACs with $\eta < 0.37$ V (NiPd, CuPd, CuPt, NiPt, CoPd, NiCu, CuCu and CoCu). According to the volcano-shaped relationship, a strong combination of $*OH-*OH$ species in the left branch caused the $*O-*O$ coupling hardly achieved, resulting in the O_2 production as PDS. Conversely, the adsorption of $*OH$ or $*OH-*OH$ as PDS in the right branch implies that too weak
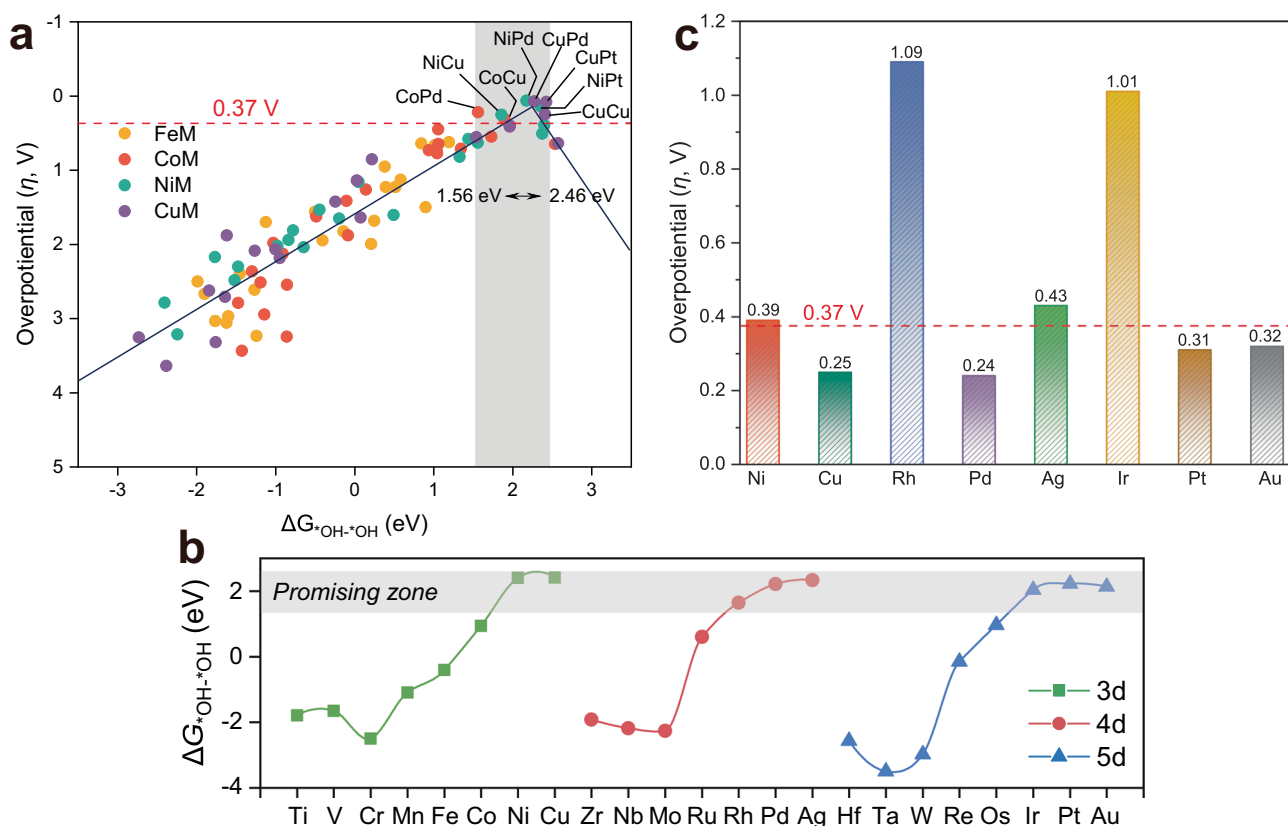
Fig. 5 | Volcano-shaped relationship and predicted reaction activity of homonuclear DACs. a Volcano-shaped relationship between the adsorption-free energy of oxygenated intermediates ($\Delta G_{*OH-*OH}$) and the theoretical overpotential (η). **b** Variations of $\Delta G_{*OH-*OH}$ on 23 homonuclear M_2@NC. **c** The η of eight promising M_2@NC homonuclear DACs are summarized in terms of $\Delta G_{*OH-*OH}$ as the activity descriptor.

binding of *OH−*OH species with the active site prevents the adsorption of *O or *OH−*OH. Consequently, to balance both aspects the optimization of the $\Delta G_{*OH-*OH}$ through adjustment of the electronic structure enables to acquire of superior active catalysts.

Using the above $\Delta G_{*OH-*OH}$ as the activity descriptor, we extended our investigation to 23 homonuclear M_2@NC to validate this screening criterion. Figure 5b shows that eight of the 23 homonuclear M_2@NC were recognized as promising candidates, which were further analyzed with more details of catalytic activity. Ultimately, DFT calculations in Fig. 5c and Supplementary Fig. 13 confirmed four homonuclear M_2@NC with η below 0.37 V: 0.24 V (Pd$_2$@NC) < 0.25 V (Cu$_2$@NC) < 0.31 V (Pt$_2$@NC) < 0.32 V (Au$_2$@NC), and the stability, optimized structures and the computed thermodynamic properties of oxygenated intermediates are given in Supplementary Fig. 14 and Supplementary Tables 61−69, respectively. Nevertheless, among the four excluded M_2@NC, Ni$_2$@NC, and Ag$_2$@NC approximated very closely to the criterion of 0.37 V as well, which illustrates the validity of the screening range of OCM from 1.56 to 2.46 eV. More importantly, this established descriptor could be used to accelerate developing more efficient catalysts, remarkably saving computational resources.

Conditions for OCM and OER activity origin
All of the above calculations demonstrate that OCM is ideal for designing high-performance OER electrocatalysts. Here, critical questions are raised: is OCM suitable for all dual metal active sites? What is the condition that triggers the occurrence of OCM? Whether the crossings of two different mechanisms happen? To answer these questions, 105 DACs, including homonuclear composition, were explored in detail. The competition between second *OH adsorption and *OH deprotonation distinguished the two mechanisms, which was

first assessed by comparing Gibbs free energy change. Figure 6a and Supplementary Tables 70−74 show that 6 heteronuclear and 4 homonuclear highly active DACs screened prefer second *OH adsorption (except for CoCu) over competitive *OH deprotonation, suggesting that these DACs are selective for *OH−*OH rather than *O. Subsequently, based on a recent study[55], DACs with *OH−*OH selectivity were further analyzed to evaluate the possibility of intermediate crossover (*OH−*OH → *OH−*O or *OH−*OH → *OOH). Figure 6b and Supplementary Tables 75−79 show that all DACs with *OH−*OH selectivity proceed along the OCM without *OOH generation. This is because the *OH−*O conformation is energetically more stable than *OOH on the metal dimer structure, which explains the scaling relationship of OCM deviating from AEM in Fig. 4b. Notably, the absence of synergistic effects in the active center of SACs caused a different scaling relationship between *OH and *OH−*O along the OCM, without overlapping with that of DACs (Supplementary Fig. 15), which resulted in a complicated OER reaction network of the SACs.

For the DACs with *O selectivity in Fig. 6a, the intricate case of crossing intermediates between OCM and AEM induces the reaction to follow a hybrid pathway (*OH → *O → *OH−*O → *O$_2$ → O$_2$(g)). For the examples of DACs with *O selectivity shown in Supplementary Fig. 16 (selected as ΔG(*OH−*O) > 0, Supplementary Tables 70−73), the PDS of all DACs except CoAu is *OH−*O → *O$_2$, and hybrid mechanism for crossing intermediates are only effective for ΔG(*OH → *O) and ΔG(*O → *OH−*O), therefore with limited effect on the catalytic activity of DACs with *O selectivity. Remarkably, the PDS of CoAu didn't occur at *OH−*O → *O$_2$, which enabled the reaction to bypass the PDS of *OH → *OH−*OH ($\Delta G = 1.88$ eV), reducing the PDS to 1.25 eV (Supplementary Fig. 16c). This indicates that the increase in OER reactivity is feasible for CoAu via the crossing between OCM and AEM
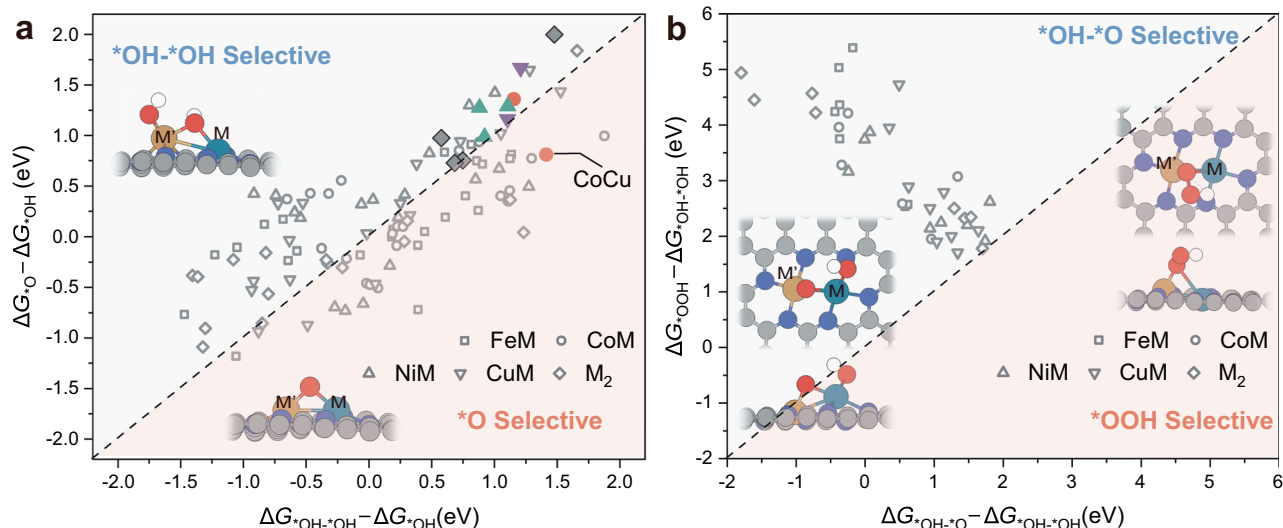
Fig. 6 | Conditions for OCM. a Gibbs free energy change (ΔG) of *OH toward *OH–*OH versus *OH → *O + H$^+$ + e$^-$. Data points screened for high-performance homo- and hetero-nuclear catalysts are colored. **b** Gibbs free energy change (ΔG) of *OH–*OH → *OH–*O + H$^+$ + e − versus *OH–*OH → *OOH + H$^+$ + e$^-$. Insets show the schematic configuration of the different intermediates adsorbed on M′M@NC. The white, red, gray, and blue spheres in the atomic models represent H, O, C, and N atoms, respectively.

intermediates. Additionally, the kinetic process of *O–*O coupling is also critical for triggering OCM, and higher kinetic barriers reduce the potential for OCM to occur. Therefore, we further calculated the possible coupling processes based on the 8 heteronuclear DACs screened (Supplementary Fig. 17 and Table 80). The results show that all 8 DACs possessed low coupling barriers and by the same magnitude as reported in the literature[48]. As a result, *O–*O coupling cannot hinder OCM from proceeding.

A critical question arises here: given that approximately half of the DACs exhibited *O selectivity, is it still valid to use $\Delta G_{*OH–*OH}$ in Fig. 5a as a descriptor to assess their reactivity? On the one hand, $\Delta G_{*OH–*OH}$ is generally applicable to OER processes along the OCM, and a secondary screening enables further rigorous identification of high-performance DACs with *O selectivity along hybrid mechanisms (e.g. CoCu). On the other hand, the fact that the $\Delta G_{*OH}/\Delta G_{*OH–*OH}$ scaling relationship and that of $\Delta G_{*OH}/\Delta G_{*O}$ virtually overlap rendered the DACs with ΔG_{*O} as descriptor still positioned on the original volcano curve (Supplementary Fig. 18). In other words, the volcano plot derived from $\Delta G_{*OH–*OH}$ with the screening scope from 1.56 to 2.46 eV still roughly determines the *O-selective DACs (e.g. CoAu) with regard to such accuracy, and the poorly active *O-selective DACs can be eliminated.

The adsorption of *OH not only plays a crucial role in determining the reaction mechanism but also the moderate adsorption strength can promote the same magnitude of free energy change for all the elementary steps, which approaches the ideal OER catalyst, rather than too strong/weak adsorption. Therefore, the DACs identified above with high OER activity should possess moderate interactions between intermediates and active sites. Here, we take the most active NiPd@NC as an example, the synergistic effect between metal dimers can be reflected in two aspects: (i) the modulation of the intrinsic electronic structure by introduction or substitution of additional metal atoms and (ii) the effect on the adsorption of the critical oxygenated intermediate *OH during the reaction.

First, we compared the density of states (DOS) of the most active NiPd@NC with the corresponding SACs (Ni@NC and Pd@NC). As shown in Supplementary Fig. 19a, the introduction of additional metal atoms seems to have a limited effect on the shape of the DOS, but the formation of M$_2$ dimers enables stronger adsorption of *OH than that of Ni@NC and Pd@NC, due to the charge redistribution bringing the DOS closer to the Fermi energy level (E_f) as shown in Supplementary

Fig. 19c, and causing the d-band center to shift upward. Also, for homonuclear combinations (Ni$_2$@NC or Pd$_2$@NC), the moderate modification of the electronic structure by the substitution of one atom leads to the alteration of the d-band center, e.g., the replacement of Pd in Pd$_2$@NC by Ni remarkably enhances the adsorption of *OH by the NiPd dimer from 1.47 to 1.29 eV (Supplementary Fig. 20).

The effect of the d-band center on the oxygenated intermediate *OH is reflected in the binding strength of metal−O bonds. Therefore, the bonding and antibonding states of *OH adsorption on the active centers of SACs and DACs were further analyzed by the crystal orbital Hamilton population (COHP) (Supplementary Fig. 19b). In contrast to Ni@NC and Pd@NC, the energy of the bonding state with NiPd@NC gradually shifted away from E_f and the filling of the antibonding orbitals gradually decreased, which contributed to the increase of the *OH adsorption strength. To gain quantitative insight into the d−2p interaction, the integrated crystal orbital Hamiltonian population (ICOHP) analysis was calculated by integrating the states of the highest occupied energy levels. Interestingly, excellent linear correlations between ΔG_{*OH} values and ICOHP, as well as the d-band center, were observed (blue line in Supplementary Fig. 21), which shows that the closer d-band center to E_f leads to the stronger *OH binding with more contribution from the occupied bonding states. This linear correlation quantitatively demonstrates that the synergistic interaction can readily adjust their electronic structures by d-band center and the adsorption nature of active sites, which are highly related to the intrinsic OER activity observed in Fig. 3d and Supplementary Fig. 20. The electronic structures of NiPt, CuPd, and CuPt also have similar phenomena and regularities, as shown in Supplementary Fig. 22.

In addition, we further extended to the remaining 10 high-performance DACs, where a similar linear correlation of ΔG_{*OH} and the d-band center was observed. It is worth noting that the d-band center for Cu-containing dimers (red line in Supplementary Fig. 21a) is much more negative and deviating severely from that of NiM dimers. This could be due to the neglected effect of the d-band shape and the sp orbitals of the metal sites[83,84], which further resulted in the opposite trend in the correlation of ΔG_{*OH} and ICOHP (red line in Supplementary Fig. 21b). Notwithstanding, it is evident that the synergistic effect of metal−metal sites render the possibility to regulate the electronic structure and d-band center. This consequently enables the binding intensity of *OH to the active site within a mild range

(−1.70 < ICOHP < −1.20 for high-performance M_2 dimers, except Au_2) and detrimental to deprotonation, thus eventually benefiting the Gibbs free energy barriers of all four elementary steps to be closer to the ideal 1.23 eV. We also plotted the M1−M2 distance versus η, as shown in Supplementary Fig. 23, with the appropriate range favoring the occurrence of OCM.

pH-dependent and potential-dependent OER activity

The above results based on conventional constant charge methods (CCM) demonstrate that the synergistic effect between the dual-metal active sites in DACs can enhance OER activity. To better simulate the electrochemical interface and to examine the effect of pH as well as potential on the reaction activity, we took advantage of the JDFTx code of the grand canonical DFT (GC-DFT) for the constant potential method (CPM) calculations[85], which have been proved useful in recent electrochemical studies[86,87]. As an example, with the screened high-performance NiPd@NC, CuPd@NC, and CuPt@NC, we adjusted the absolute electrode potential to change the pH and electrochemical interface potential (referenced to RHE) as shown in Fig. 7 and

Supplementary Tables 81–83. Interestingly, the activity order evaluated by the two methods of CCM (Fig. 3) and CPM was consistent for the three DACs under alkaline conditions. In addition, the change in pH triggered a change in PDS, rendering the higher η for CuPd than CuPt under acidic conditions. The order of η for these three DACs is 0.08 V (NiPd) < 0.18 V (CuPt) < 0.20 V (CuPd) in acidic conditions, and 0.10 V (NiPd) < 0.18 V (CuPd) < 0.28 V (CuPt) in alkaline conditions, respectively, indicating they are all potentially promising catalysts via OCM under both acidic and alkaline conditions.

As shown in Fig. 7a–f, the free energy changes (ΔG) of the elementary steps decreases as the applied potential increases until the overpotential is determined with the maximum $\Delta G = 0$ (Supplementary Fig. 24), and this is analogous to a recent study of $(phen_2N_2)FeCl$ monolayer[88]. Furthermore, the PDS of the three DACs is $*OH-*O \rightarrow *O_2$ (for NiPd@NC and CuPd@NC at pH = 1, it is $*OH-*OH \rightarrow *OH-*O$). The difference in activity of the three DACs derived from the different sensitivity of their oxygenated intermediates to the electrical potential, with the $*OH-*O$ species being more significant (Supplementary Fig. 24). The decreasing trend of ΔG ($*OH *O \rightarrow *O_2$) can be prominently
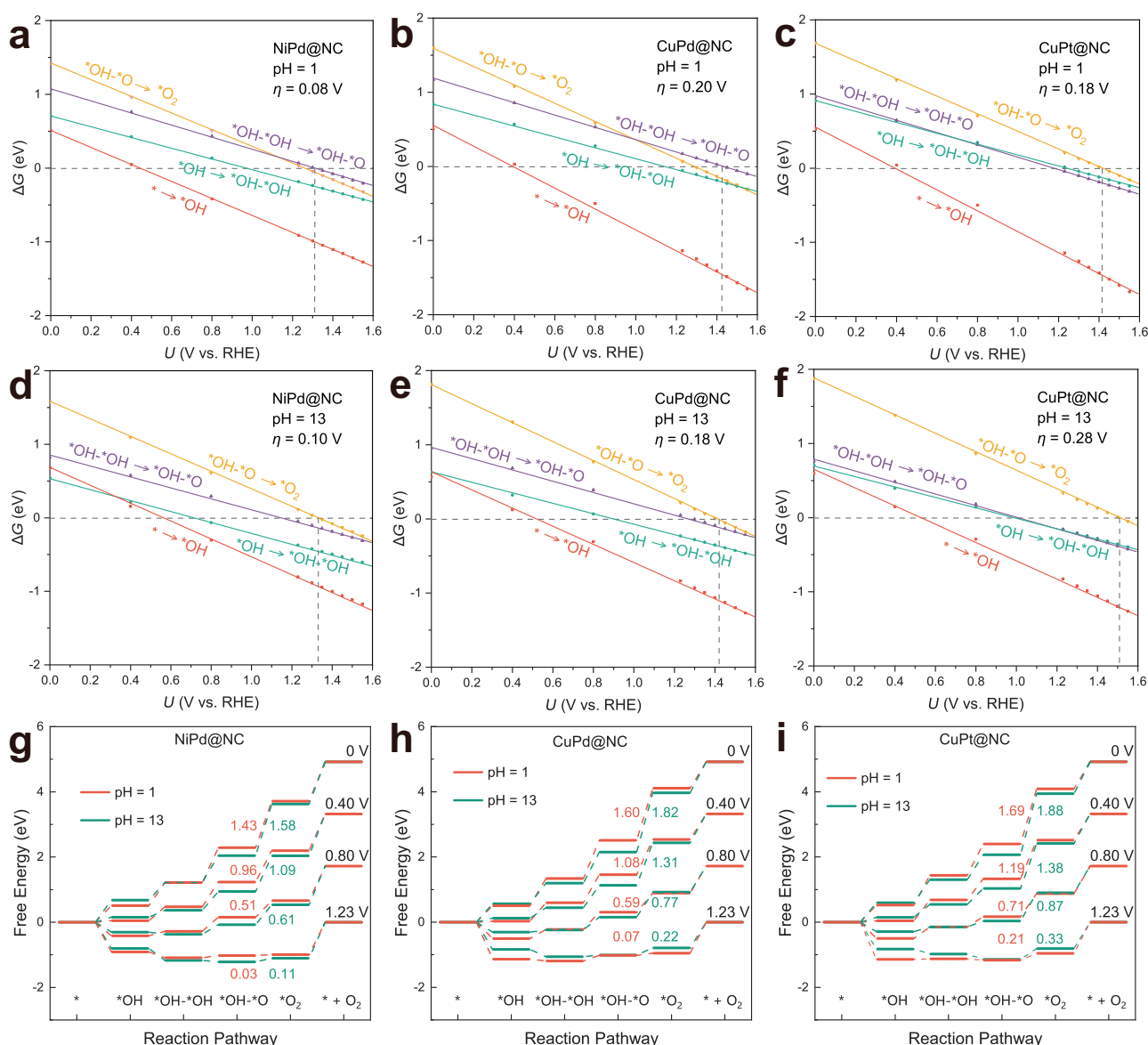

Fig. 7 | Free energy diagrams for pH-dependent and potential-dependent. Variation of Gibbs free energy with potential for **a** NiPd@NC, **b** CuPd@NC, and **c** CuPt@NC at pH = 1. Variation of Gibbs free energy with potential for **d** NiPd@NC,

e CuPd@NC, and **f** CuPt@NC at pH = 13. Free energy diagrams of **g** NiPd@NC, **h** CuPd@NC, and **i** CuPt@NC at different potentials with pH = 1 and 13, and the corresponding $\Delta G_{*OH-*O \rightarrow *O2}$ are labeled.

observed in Fig. 7g–i with the gradual application of electrical potential. In terms of pH, another critical factor affecting activity, the considerable difference of 0.1 V in the overpotential of CuPt@NC under acidic and alkaline conditions can be attributed to the shift in the relative location of *OH–*O → *O₂ (as denoted by the yellow lines in Fig. 7c and f). The PDS of NiPd@NC and CuPd@NC altered from *OH–*O → *O₂ to *OH–*OH → *OH–*O as the alkaline to acidic conditions changed (Fig. 7a and b). Consequently, both pH and potential have significant contributions to the electrochemical process, with the influence on the PDS and overpotential. Nevertheless, the superior OER activity for the screened three DACs can be appraised.

Discussion
In summary, we employed M′M@NC catalyst as a prototype to explore the activity and feasibility of OER along the OCM on the dual-metal active site. Large-scale screening constructed activity maps and predicted NiPd@NC (0.06 V), CuPd@NC (0.07 V), and CuPt@NC (0.08 V) significantly lower than the bottleneck 0.37 V of conventional AEM. The more favorable configuration of adsorption on the M₂ dimer for two *OH, which tactfully circumvents the scaling relationship between *OOH and *OH, renders η closer to the ideal 0 V. Further, rationally constructed descriptor $\Delta G_{*OH-*OH}$ for the prediction of homonuclear compositions verified the effectiveness of the design strategy. More importantly, the feasible occurrence of OCM could be assessed based on the Gibbs free energy barriers of the two competing reactions (*OH → *OH–*OH vs. *OH → *O). We further demonstrated that the synergistic effect between M₂ dimers efficiently modulates the d-band center as well as the bonding/anti-bonding state of M–O bonds to facilitate the moderate adsorption of *OH, thus enabling high-performance DACs via OCM. This work provides a comprehensive understanding of the OCM mechanism, rendering an alternative recipe for the catalytic optimization of OER, with a volcano top different from that of conventional AEM. Further, CPM considering surface charge reveals pH-dependent and potential-dependent OER activity on diatomic catalysts, indicating the selected three DACs of NiPd@NC, CuPd@NC, and CuPt@NC are promising candidates under both acidic and alkaline conditions. It is important that OCM should be considered as a prominent OER pathway catalyzed by DACs in future studies. These theoretical insights would be also beneficial in designing high-performance catalysts for other electrochemical reactions.
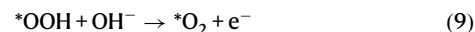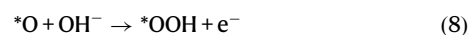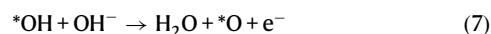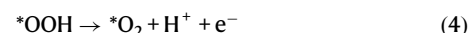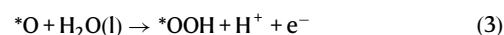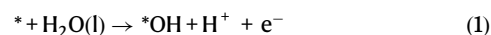
Methods
DFT calculations
All spin-polarized density functional theory (DFT) calculations were performed using VASP 6.2.0 code[89]. The exchange-correlation function was employed to accurately simulate the interactions between electrons, which is described by the Perdew–Burke–Ernzerhof (PBE)[90] within the generalized gradient approximation (GGA-PBE). Taking 450 eV as the structural relaxation cutoff energy and the Gaussian smearing with $k_B T = 0.05$ eV to accelerate convergence, the core −valence interactions in the system were described in terms of the projector augmented wave (PAW) pseudopotential[91,92]. A series of Fe-, Co-, Ni-, and Cu-based heteronuclear and homonuclear metal dimers are embedded in N-doped graphene (NC), which were built based on a $p(6 × 6)$ monolayer of pristine graphene, for which M@NC was constructed using a $p(5 × 5)$ monolayer slab. A vacuum layer with a distance of 15 Å was employed in the vertical direction of the two-dimensional monolayer to avoid the interaction between two adjacent periodic images. The Γ-centered Monkhorst–Pack scheme[93] with 3 × 3 × 1 and 5 × 5 × 1 k-points grids was adopted to sample the Brillouin zone in the reciprocal space for geometric optimization and electronic structure calculations, respectively. The ionic optimization is performed using the conjugate gradient algorithm with the electron relaxation convergence threshold set to 10^{-5} eV and the Hellmann-Feynman force convergence threshold set to 0.01 eV/Å. In addition, the solvation effect
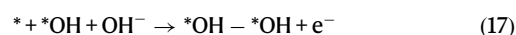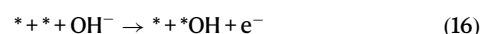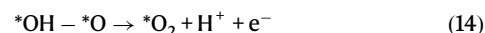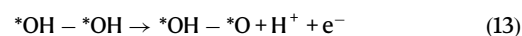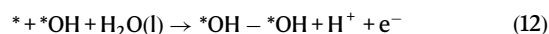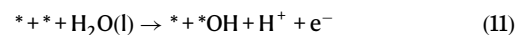
of water was simulated with the implicit Poisson−Boltzmann solvation model of VASPsol[94], and the long-range van der Waals interactions were performed using empirical dispersion (DFT-D2)[95]. The calculation of the charge transfer between atoms was adapted from the Bader charge analysis method[96]. The VASPKIT code was used to post-process the results of the VASP calculations[97]. The climbing image nudged elastic band (CI-NEB) method[98] combined with improved dimer method (IDM)[99] was employed to searched for transition states (TS).
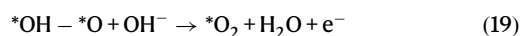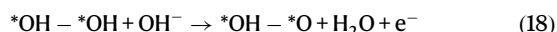
Free energy computations
The adsorption evolution mechanism (AEM) was widely accepted as a theoretical approach to mimic the OER reaction in acidic (pH = 1) and alkaline solutions (pH = 13)[100], which can be described as a four-electron transfer reaction pathway with the overall reaction pathway of OER in acidic and alkaline solutions as shown in Eqs. (1)–(5) and (6)–(10), respectively:

$$* + H_2O(l) \rightarrow *OH + H^+ + e^- \tag{1}$$

$$*OH \rightarrow *O + H^+ + e^- \tag{2}$$

$$*O + H_2O(l) \rightarrow *OOH + H^+ + e^- \tag{3}$$

$$*OOH \rightarrow *O_2 + H^+ + e^- \tag{4}$$

$$*O_2 \rightarrow O_2(g) + * \tag{5}$$

$$* + OH^- \rightarrow *OH + e^- \tag{6}$$

$$*OH + OH^- \rightarrow H_2O + *O + e^- \tag{7}$$

$$*O + OH^- \rightarrow *OOH + e^- \tag{8}$$

$$*OOH + OH^- \rightarrow *O_2 + e^- \tag{9}$$

$$*O_2 \rightarrow O_2(g) + * \tag{10}$$

where *, *OH, *O, *OOH, and *O₂ denote adsorbed sites, adsorbed oxygenated intermediate species OH, O, OOH, and O₂, respectively. In addition, the *O–*O coupling mechanism (OCM) on dual-metal active sites in acidic (Eqs. (11)–(15)) and alkaline solutions (Eqs. (16)–(20)) is a feasible reaction pathway[48]:

$$* + * + H_2O(l) \rightarrow * + *OH + H^+ + e^- \tag{11}$$

$$* + *OH + H_2O(l) \rightarrow *OH - *OH + H^+ + e^- \tag{12}$$

$$*OH - *OH \rightarrow *OH - *O + H^+ + e^- \tag{13}$$

$$*OH - *O \rightarrow *O_2 + H^+ + e^- \tag{14}$$

$$*O_2 \rightarrow * + * + O_2(g) \tag{15}$$

$$* + * + OH^- \rightarrow * + *OH + e^- \tag{16}$$

$$* + *OH + OH^- \rightarrow *OH - *OH + e^- \tag{17}$$

$$*OH - *OH + OH^- \rightarrow *OH - *O + H_2O + e^- \tag{18}$$

$$*OH - *O + OH^- \rightarrow *O_2 + H_2O + e^- \tag{19}$$

$$*O_2 \rightarrow * + * + O_2(g) \tag{20}$$

where $*O_2$ includes the side-on configuration ($*O-O*$) as well as the end-on configuration ($*OO$), both of which employed the most stable configuration of the adsorbed O_2 in the calculations. The free energy diagrams of the OER elementary steps involving ($H^+ + e^-$) pair transfer as proposed by Nørskov and co-workers were calculated using the computational hydrogen electrode (CHE) model[101]. The Gibbs free energy (ΔG) changes for each elementary step are given as follows:

$$\Delta G = \Delta E + \Delta E_{ZPE} - T\Delta S + \Delta G_U + \Delta E_{sol} \tag{21}$$

where ΔE is the total energy of the reaction under vacuum conditions calculated by DFT, with ΔE_{ZPE} and $T\Delta S$ representing the zero-point energy change based on the calculated vibrational frequency and the entropy change at a reaction temperature at $T = 298.15\,K$, respectively. The values of E_{ZPE} and TS for H_2O and H_2 can be seen in Supplementary Table 1. The water dielectric constant ($\varepsilon = 80$) was adopted to take into account the effect of the solvent on oxygenated intermediates and is denoted by ΔE_{sol}. $\Delta G_U = -neU$ is the contribution of the applied electrode potential to the reaction Gibbs free energy, where n and U are the number of transferred ($H^+ + e^-$) pairs and the applied electrode potential versus the reversible hydrogen electrode (RHE) for each elementary reaction, respectively. In addition, the energy of the open-shell triplet ground state O_2 molecule is derived as $G_{O2} = 2G_{H2O} - 2G_{H2} + 4.92\,eV$ due to the inability of DFT to precisely calculate the energy of the O_2 molecule, while the entropy of the gaseous molecules (H_2 and H_2O) was taken from the NIST Chemistry WebBook[102]. For OCM the Gibbs free energy of the elementary steps is calculated as

$$\Delta G_1 = \Delta G_{*OH} - eU \tag{22}$$

$$\Delta G_2 = \Delta G_{*OH-*OH} - \Delta G_{*OH} - eU \tag{23}$$

$$\Delta G_3 = \Delta G_{*OH-*O} - \Delta G_{*OH-*OH} - eU \tag{24}$$

$$\Delta G_4 = \Delta G_{*O2} - \Delta G_{*OH-*O} - eU \tag{25}$$

$$\Delta G_5 = 4.92\,eV - \Delta G_{*O2} \tag{26}$$

The theoretical overpotential was derived from the following equation:

$$\eta = max[\Delta G_1, \Delta G_2, \Delta G_3, \Delta G_4]/e - 1.23\,V \tag{27}$$

Constant-potential calculations

The grand canonical ensemble DFT simulations were performed using the JDFTx software[85], and the electron exchange-correlation energy was evaluated within the GGA-PBE functional, consistent with the calculation in VASP. The GBRV pseudopotentials and a plane wave energy cut-off of 20 Hartree was employed. The linear PCM solvation model (CANDLE) simulates the liquid environment, with $0.1\,M\,K^+$ and F^- ions[103]. The Brillouin zone was sampled using a $2 \times 2 \times 1$ Monkhorst−Pack k-point mesh and a convergence threshold of 1×10^{-6}

Hartree was set for the total electronic energy. The effective regulation of pH and potential can be described by the following relation:

$$U(V/RHE) = U(V/SHE) + 0.0592 \times pH \tag{28}$$

$$U(V/SHE) = -4.66\,V - U_{applied}(V/SHE) \tag{29}$$

where $-4.66\,V$ is the absolute electrode potential with SHE as reference[104], and the $U_{applied}$ is the applied electrode potentials of the targets.

Data availability

The data that support the findings of this study are available from the corresponding author upon request. Source data are provided with this paper. The atomic coordinates of the optimized model for electronic structure calculations are provided as a separate Supplementary Data 1. Source data are provided with this paper.

References

1. Wei, C. et al. Recommended practices and benchmark activity for hydrogen and oxygen electrocatalysis in water splitting and fuel cells. *Adv. Mater.* **31**, 1806296 (2019).
2. Cao, R., Lee, J.-S., Liu, M. & Cho, J. Recent progress in non-precious catalysts for metal–air batteries. *Adv. Energy Mater.* **2**, 816–829 (2012).
3. Fu, J. et al. Electrically rechargeable zinc-air batteries: progress, challenges, and perspectives. *Adv. Mater.* **29**, 1604685 (2017).
4. Mefford, J. T. et al. Correlative operando microscopy of oxygen evolution electrocatalysts. *Nature* **593**, 67–73 (2021).
5. Song, F. et al. Transition metal oxides as electrocatalysts for the oxygen evolution reaction in alkaline solutions: an application-inspired renaissance. *J. Am. Chem. Soc.* **140**, 7748–7759 (2018).
6. Jiao, Y., Zheng, Y., Jaroniec, M. & Qiao, S. Z. Design of electro-catalysts for oxygen- and hydrogen-involving energy conversion reactions. *Chem. Soc. Rev.* **44**, 2060–2086 (2015).
7. Sanchez Casalongue, H. G. et al. In situ observation of surface species on iridium oxide nanoparticles during the oxygen evolution reaction. *Angew. Chem. Int. Ed.* **53**, 7169–7172 (2014).
8. Lee, Y., Suntivich, J., May, K. J., Perry, E. E. & Shao-Horn, Y. Synthesis and activities of rutile IrO_2 and RuO_2 nanoparticles for oxygen evolution in acid and alkaline solutions. *J. Phys. Chem. Lett.* **3**, 399–404 (2012).
9. Montoya, J. H. et al. Materials for solar fuels and chemicals. *Nat. Mater.* **16**, 70–81 (2016).
10. Yu, Z. Y. et al. Clean and affordable hydrogen fuel from alkaline water splitting: past, recent progress, and future prospects. *Adv. Mater.* **33**, 2007100 (2021).
11. Wang, Y. et al. Advanced electrocatalysts with single-metal-atom active sites. *Chem. Rev.* **120**, 12217–12314 (2020).
12. Fang, C. & An, W. Single-metal-atom site with high-spin state embedded in defective BN nanosheet promotes electrocatalytic nitrogen reduction. *Nano Res.* **14**, 4211–4219 (2021).
13. Zhao, C. X., Li, B. Q., Liu, J. N. & Zhang, Q. Intrinsic electrocatalytic activity regulation of M–N–C single-atom catalysts for the oxygen reduction reaction. *Angew. Chem. Int. Ed.* **60**, 4448–4463 (2021).
14. Wang, T. et al. Carbon-rich nonprecious metal single atom electrocatalysts for CO_2 reduction and hydrogen evolution. *Small Methods* **3**, 1900210 (2019).
15. Zhang, C. et al. Single-atom catalysts for hydrogen generation: rational design, recent advances, and perspectives. *Adv. Energy Mater.* **12**, 2200875 (2022).
16. Liu, S. et al. Atomically dispersed iron sites with a nitrogen–carbon coating as highly active and durable oxygen reduction catalysts for fuel cells. *Nat. Energy* **7**, 652–663 (2022).

17. Zhang, J., Yang, H. & Liu, B. Coordination engineering of single-atom catalysts for the oxygen reduction reaction: a review. *Adv. Energy Mater.* **11**, 2002473 (2020).

18. Xiao, M. et al. Engineering energy level of metal center: Ru single-atom site for efficient and durable oxygen reduction catalysis. *J. Am. Chem. Soc.* **141**, 19800–19806 (2019).

19. Leverett, J. et al. Tuning the coordination structure of Cu–N–C single atom catalysts for simultaneous electrochemical reduction of CO_2 and NO_3^- to urea. *Adv. Energy Mater.* **12**, 2201500 (2022).

20. Zhou, Y. et al. Recent advances in single-atom electrocatalysts supported on two-dimensional materials for the oxygen evolution reaction. *J. Mater. Chem. A* **9**, 9979–9999 (2021).

21. Li, M. et al. Heterogeneous single-atom catalysts for electro-chemical CO_2 reduction reaction. *Adv. Mater.* **32**, 2001848 (2020).

22. Chen, J. et al. Promoting electrochemical CO_2 reduction via boosting activation of adsorbed intermediates on iron single-atom catalyst. *Adv. Funct. Mater.* **32**, 2110174 (2022).

23. Zhang, J., Cai, W., Hu, F. X., Yang, H. & Liu, B. Recent advances in single atom catalysts for the electrochemical carbon dioxide reduction reaction. *Chem. Sci.* **12**, 6800–6819 (2021).

24. Wang, B., Chen, S., Zhang, Z. & Wang, D. Low-dimensional mate-rial supported single-atom catalysts for electrochemical CO_2 reduction. *SmartMat* **3**, 84–110 (2022).

25. Sun, Q., Jia, C., Zhao, Y. & Zhao, C. Single atom-based catalysts for electrochemical CO_2 reduction. *Chin. J. Catal.* **43**, 1547–1597 (2022).

26. Tang, T., Wang, Z. & Guan, J. Optimizing the electrocatalytic selectivity of carbon dioxide reduction reaction by regulating the electronic structure of single-atom M–N–C materials. *Adv. Funct. Mater.* **32**, 2111504 (2022).

27. Li, R. & Wang, D. Understanding the structure-performance rela-tionship of active sites at atomic scale. *Nano Res.* **15**, 6888–6923 (2022).

28. Exner, K. S. Why the breaking of the OOH versus OH scaling relation might cause decreased electrocatalytic activity. *Chem. Catal.* **1**, 258–271 (2021).

29. Pérez-Ramírez, J. & López, N. Strategies to break linear scaling relationships. *Nat. Catal.* **2**, 971–976 (2019).

30. Zhang, H., Jin, X., Lee, J. M. & Wang, X. Tailoring of active sites from single to dual atom sites for highly efficient electrocatalysis. *ACS Nano* **16**, 17572–17592 (2022).

31. Li, Y. et al. Synergistic effect of atomically dispersed Ni–Zn pair sites for enhanced CO_2 electroreduction. *Adv. Mater.* **33**, 2102212 (2021).

32. Cao, Y. et al. Hydrogen peroxide electrochemical synthesis on hybrid double-atom (Pd–Cu) doped N vacancy g-C_3N_4: a novel design strategy for electrocatalyst screening. *J. Mater. Chem. A* **8**, 2672–2683 (2020).

33. Zhu, X. et al. Activity origin and design principles for oxygen reduction on dual-metal-site catalysts: a combined density func-tional theory and machine learning study. *J. Phys. Chem. Lett.* **10**, 7760–7766 (2019).

34. Li, X., Zhong, W., Cui, P., Li, J. & Jiang, J. Design of efficient cata-lysts with double transition metal atoms on C_2N Layer. *J. Phys. Chem. Lett.* **7**, 1750–1755 (2016).

35. Wang, S. et al. Highly efficient photo-/electrocatalytic reduction of nitrogen into ammonia by dual-metal sites. *ACS Cent. Sci.* **6**, 1762–1771 (2020).

36. Lv, X., Wei, W., Huang, B., Dai, Y. & Frauenheim, T. High-throughput screening of synergistic transition metal dual-atom catalysts for efficient nitrogen fixation. *Nano Lett.* **21**, 1871–1878 (2021).

37. Zhang, J. & An, W. Single-, double-, and triple-atom catalysts on graphene-like C_2N enable electrocatalytic nitrogen reduction: Insight from first principles. *Catal. Sci. Technol.* **12**, 2604–2617 (2022).

38. Liu, X., Jiao, Y., Zheng, Y., Davey, K. & Qiao, S.-Z. A computational study on Pt and Ru dimers supported on graphene for the hydrogen evolution reaction: New insight into the alkaline mechanism. *J. Mater. Chem. A* **7**, 3648–3654 (2019).

39. Zhang, X., Chen, A., Zhang, Z., Jiao, M. & Zhou, Z. Transition metal anchored C_2N monolayers as efficient bifunctional electro-catalysts for hydrogen and oxygen evolution reactions. *J. Mater. Chem. A* **6**, 11446–11452 (2018).

40. Liu, H. et al. Dual-atom active sites embedded in two-dimensional C_2N for efficient CO_2 electroreduction: a computational study. *J. Energy Chem.* **61**, 507–516 (2021).

41. Ouyang, Y., Shi, L., Bai, X., Li, Q. & Wang, J. Breaking scaling relations for efficient CO_2 electrochemical reduction through dual-atom catalysts. *Chem. Sci.* **11**, 1807–1813 (2020).

42. Karmodak, N., Vijay, S., Kastlunger, G. & Chan, K. Computational screening of single and di-atom catalysts for electrochemical CO_2 reduction. *ACS Catal.* **12**, 4818–4824 (2022).

43. Han, X. et al. Atomically dispersed binary Co–Ni sites in nitrogen-doped hollow carbon nanocubes for reversible oxygen reduction and evolution. *Adv. Mater.* **31**, 1905622 (2019).

44. Wei, Y. S. et al. Fabricating dual-atom iron catalysts for efficient oxygen evolution reaction: a heteroatom modulator approach. *Angew. Chem. Int. Ed.* **59**, 16013–16022 (2020).

45. Zhu, X. et al. Harnessing the interplay of Fe–Ni atom pairs embedded in nitrogen-doped carbon for bifunctional oxygen electrocatalysis. *Nano Energy* **71**, 104597 (2020).

46. Pei, Z. et al. Highly efficient electrocatalytic oxygen evolution over atomically dispersed synergistic Ni/Co dual sites. *Angew. Chem. Int. Ed.* **61**, 202207537 (2022).

47. Pan, F. et al. Theory-guided design of atomic Fe–Ni dual sites in N,P-co-doped C for boosting oxygen evolution reaction. *Chem. Catal.* **1**, 734–745 (2021).

48. Zhang, C., Qin, S., Li, B. & Jin, P. Dual-metal atom incorporated N-doped graphenes as oxygen evolution reaction electro-catalysts: high activities achieved by site synergies. *J. Mater. Chem. A* **10**, 8309–8323 (2022).

49. Yang, C. et al. Electronic properties of double-atom catalysts for electrocatalytic oxygen evolution reaction in alkaline solution: a DFT study. *Nanoscale* **14**, 187–195 (2021).

50. Zhang, L., Guo, X., Zhang, S. & Huang, S. Building up the "gen-ome" of bi-atom catalysts toward efficient HER/OER/ORR. *J. Mater. Chem. A* **10**, 11600–11612 (2022).

51. Wu, L., Guo, T. & Li, T. Data-driven high-throughput rational design of double-atom catalysts for oxygen evolution and reduction. *Adv. Funct. Mater.* **32**, 2203439 (2022).

52. Zhou, Y. et al. Dual-metal atoms embedded into two-dimensional covalent organic framework as efficient electrocatalysts for oxy-gen evolution reaction: a DFT study. *Nano Res.* **15**, 7994–8000 (2022).

53. Di Liberto, G., Cipriano, L. A. & Pacchioni, G. Role of dihydride and dihydrogen complexes in hydrogen evolution reaction on single-atom catalysts. *J. Am. Chem. Soc.* **143**, 20431–20441 (2021).

54. Zhong, L. & Li, S. Unconventional oxygen reduction reaction mechanism and scaling relation on single-atom catalysts. *ACS Catal.* **10**, 4313–4318 (2020).

55. Barlocco, I., Cipriano, L. A., Di Liberto, G. & Pacchioni, G. Does the oxygen evolution reaction follow the classical OH*, O*, OOH* path on single atom catalysts? *J. Catal.* **417**, 351–359 (2023).

56. Cipriano, L. A., Di Liberto, G. & Pacchioni, G. Superoxo and peroxo complexes on single-atom catalysts: Impact on the oxygen evo-lution reaction. *ACS Catal.* **12**, 11682–11691 (2022).

57. Wan, W. et al. Mechanistic insight into the active centers of single/dual-atom Ni/Fe-based oxygen electrocatalysts. *Nat. Commun.* **12**, 5589 (2021).

58. Zhang, N. et al. Lattice oxygen activation enabled by high-valence metal sites for enhanced water oxidation. *Nat. Commun.* **11**, 4066 (2020).

59. Huang, Z.-F. et al. Chemical and structural origin of lattice oxygen oxidation in Co–Zn oxyhydroxide oxygen evolution electrocatalysts. *Nat. Energy* **4**, 329–338 (2019).

60. Song, J. et al. A review on fundamentals for designing oxygen evolution electrocatalysts. *Chem. Soc. Rev.* **49**, 2196–2214 (2020).

61. Li, R. & Wang, D. Superiority of dual-atom catalysts in electrocatalysis: one step further than single-atom catalysts. *Adv. Energy Mater.* **12**, 2103564 (2022).

62. An, Q. et al. Recent advances in dual-atom site catalysts for efficient oxygen and carbon dioxide electrocatalysis. *Small Methods* **6**, 2200408 (2022).

63. Zhu, J. et al. Quasi-covalently coupled Ni–Cu atomic pair for synergistic electroreduction of CO_2. *J. Am. Chem. Soc.* **144**, 9661–9671 (2022).

64. Winter, M. *WebElements* https://www.webelements.com (2022).

65. Zhu, C. et al. Establishing the principal descriptor for electrochemical urea production via the dispersed dual-metals anchored on the N-decorated graphene. *Adv. Sci.* **9**, 2105697 (2022).

66. Guo, X. et al. Tackling the activity and selectivity challenges of electrocatalysts toward the nitrogen reduction reaction via atomically dispersed biatom catalysts. *J. Am. Chem. Soc.* **142**, 5709–5721 (2020).

67. Liu, C. et al. Catalytic activity enhancement on alcohol dehydrogenation via directing reaction pathways from single- to double-atom catalysis. *J. Am. Chem. Soc.* **144**, 4913–4924 (2022).

68. Wang, J. et al. Synergistic effect of well-defined dual sites boosting the oxygen reduction reaction. *Energy Environ. Sci.* **11**, 3375–3379 (2018).

69. Yang, J. et al. A highly efficient fenton-like catalyst based on isolated diatomic Fe–Co anchored on N-doped porous carbon. *Chem. Eng. J.* **404**, 126376 (2021).

70. Yu, D. et al. Dual-sites coordination engineering of single atom catalysts for flexible metal-air batteries. *Adv. Energy Mater.* **11**, 2101242 (2021).

71. Sun, J., Gao, W., Fei, H. & Zhao, G. Efficient and selective electrochemical reduction of nitrate to N_2 by relay catalytic effects of Fe–Ni bimetallic sites on MOF-derived structure. *Appl. Catal. B* **301**, 120829 (2022).

72. Ren, W. et al. Isolated diatomic Ni–Fe metal–nitrogen sites for synergistic electroreduction of CO_2. *Angew. Chem. Int. Ed.* **58**, 6972–6976 (2019).

73. Wu, H. et al. Synergistic effects for boosted persulfate activation in a designed Fe–Cu dual-atom site catalyst. *Chem. Eng. J.* **428**, 132611 (2022).

74. Feng, M. et al. Well-defined Fe–Cu diatomic sites for efficient catalysis of CO_2 electroreduction. *J. Mater. Chem. A* **9**, 23817–23827 (2021).

75. Ye, W. et al. Precisely tuning the number of Fe atoms in clusters on N-doped carbon toward acidic oxygen reduction reaction. *Chem* **5**, 2865–2878 (2019).

76. Yang, B. et al. Nickel dual-atom catalysts for the selective electrocatalytic debromination of tribromoacetic acid as a green chemistry process. *Chem. Eng. J.* **427**, 131719 (2022).

77. Sun, M. J. et al. A highly efficient diatomic nickel electrocatalyst for CO_2 reduction. *Chem. Commun.* **56**, 8798–8801 (2020).

78. Luo, G., Jing, Y. & Li, Y. Rational design of dual-metal-site catalysts for electroreduction of carbon dioxide. *J. Mater. Chem. A* **8**, 15809–15815 (2020).

79. Zhang, B. et al. Homogeneously dispersed multimetal oxygen-evolving catalysts. *Science* **352**, 333–337 (2016).

80. Di Liberto, G., Cipriano, L. A. & Pacchioni, G. Single atom catalysts: what matters most, the active site or the surrounding? *ChemCatChem* **14**, 202200611 (2022).

81. Li, Y., Su, H., Chan, S. H. & Sun, Q. CO_2 electroreduction performance of transition metal dimers supported on graphene: a theoretical study. *ACS Catal.* **5**, 6658–6664 (2015).

82. He, Z. et al. Atomic structure and dynamics of metal dopant pairs in graphene. *Nano Lett.* **14**, 3766–3772 (2014).

83. Xin, H., Vojvodic, A., Voss, J., Nørskov, J. K. & Abild-Pedersen, F. Effects of d-band shape on the surface reactivity of transition-metal alloys. *Phys. Rev. B* **89**, 115114 (2014).

84. Niu, H. et al. Revealing the oxygen reduction reaction activity origin of single atoms supported on g-C_3N_4 monolayers: a first-principles study. *J. Mater. Chem. A* **8**, 6555–6563 (2020).

85. Sundararaman, R. et al. JDFTx: software for joint density-functional theory. *SoftwareX* **6**, 278–284 (2017).

86. Liu, C. et al. Oxygen evolution reaction over catalytic single-site Co in a well-defined brookite TiO_2 nanorod surface. *Nat. Catal.* **4**, 36–45 (2020).

87. Xie, Y. et al. High carbon utilization in CO_2 reduction to multi-carbon products in acidic media. *Nat. Catal.* **5**, 564–570 (2022).

88. Liu, T., Wang, Y. & Li, Y. Two-dimensional organometallic frameworks with pyridinic single-metal-atom sites for bifunctional ORR/OER. *Adv. Funct. Mater.* **32**, 2207110 (2022).

89. Kresse, G. & Hafner, J. Ab initio molecular dynamics for liquid metals. *Phys. Rev. B* **47**, 558–561 (1993).

90. Perdew, J. P., Burke, K. & Ernzerhof, M. Generalized gradient approximation made simple. *Phys. Rev. Lett.* **77**, 3865–3868 (1996).

91. Blöchl, P. E. Projector augmented-wave method. *Phys. Rev. B* **50**, 17953–17979 (1994).

92. Kresse, G. & Joubert, D. From ultrasoft pseudopotentials to the projector augmented-wave method. *Phys. Rev. B* **59**, 1758–1775 (1999).

93. Monkhorst, H. J. & Pack, J. D. Special points for Brillouin-zone integrations. *Phys. Rev. B* **13**, 5188–5192 (1976).

94. Mathew, K., Sundararaman, R., Letchworth-Weaver, K., Arias, T. A. & Hennig, R. G. Implicit solvation model for density-functional study of nanocrystal surfaces and reaction pathways. *J. Chem. Phys.* **140**, 9519–9825 (2014).

95. Grimme, S. Semiempirical GGA-Type density functional constructed with a long-range dispersion correction. *J. Comput. Chem.* **27**, 1787–1799 (2006).

96. Henkelman, G., Arnaldsson, A. & Jónsson, H. A fast and robust algorithm for Bader decomposition of charge density. *Comput. Mater. Sci.* **36**, 354–360 (2006).

97. Wang, V., Xu, N., Liu, J., Tang, G. & Geng, W. VASPKIT: a user-friendly interface facilitating high-throughput computing and analysis using VASP code. *Comput. Phys. Commun.* **267**, 108033 (2021).

98. Henkelman, G., Uberuaga, B. P. & Jónsson, H. A climbing image nudged elastic band method for finding saddle points and minimum energy paths. *J. Chem. Phys.* **113**, 9901–9904 (2000).

99. Henkelman, G. & Jónsson, H. A dimer method for finding saddle points on high dimensional potential surfaces using only first derivatives. *J. Chem. Phys.* **111**, 7010–7022 (1999).

100. Gao, L., Cui, X., Sewell, C. D., Li, J. & Lin, Z. Recent advances in activating surface reconstruction for the high-efficiency oxygen evolution reaction. *Chem. Soc. Rev.* **50**, 8428–8469 (2021).

101. Nørskov, J. et al. Origin of the overpotential for oxygen reduction at a fuel-cell cathode. *J. Phys. Chem. B* **46**, 17886–17892 (2004).

102. National Institute of Standards and Technology, *NIST Chemistry WebBook* https://webbook.nist.gov/chemistry/ (2022).

103. Sundararaman, R. & Goddard, W. A. The charge-asymmetric nonlocally determined local-electric (CANDLE) solvation model. *J. Chem. Phys.* **142**, 064107 (2015).
104. Trasatti, S. Structure of the metal/electrolyte solution interface: new data for theory. *Electrochim. Acta* **36**, 1659–1667 (1991).

Acknowledgements

Author contributions

X.Y.S. and C.F. conceived and directed the research. C.F. conducted the calculations and analyzed the data. W.C.W. and Y.X.D. discussed the calculation results and commented on the paper., J.Z. and L.L.Z. contributed to the discussions. C.F. prepared the manuscript with feedback from all authors.

Competing interests

The authors declare no competing interests.

Additional information

Supplementary information The online version contains supplementary material available at https://doi.org/10.1038/s41467-023-40177-1.

Correspondence and requests for materials should be addressed to Yuxiao Ding or Xiaoyan Sun.

Peer review information *Nature Communications* thanks the anonymous reviewer(s) for their contribution to the peer review of this work. A peer review file is available.

Reprints and permissions information is available at http://www.nature.com/reprints

Publisher's note Springer Nature remains neutral with regard to jurisdictional claims in published maps and institutional affiliations.